Eur. Phys. J. A **31**, 79–93 (2007)
DOI 10.1140/epja/i2006-10167-8

THE EUROPEAN PHYSICAL JOURNAL A

Regular Article – Hadron Physics

Polarization observable measurements for $\gamma p \to K^+\Lambda$ and $\gamma p \to K^+\Sigma^0$ for energies up to 1.5 GeV

A. Lleres[1,a], O. Bartalini[2,9], V. Bellini[12,5], J.P. Bocquet[1], P. Calvat[1], M. Capogni[2,9,b], L. Casano[9], M. Castoldi[7], A. D'Angelo[2,9], J.-P. Didelez[14], R. Di Salvo[9], A. Fantini[2,9], C. Gaulard[4,c], G. Gervino[3,10], F. Ghio[8,11], B. Girolami[8,11], A. Giusa[12,6], M. Guidal[14], E. Hourany[14], V. Kouznetsov[13], R. Kunne[14], A. Lapik[13], P. Levi Sandri[4], D. Moricciani[9], A.N. Mushkarenkov[13], V. Nedorezov[13], L. Nicoletti[2,9,1], C. Perrin[1], C. Randieri[12,5], D. Rebreyend[1], F. Renard[1], N. Rudnev[13], T. Russew[1], G. Russo[12,6], C. Schaerf[2,9], M.-L. Sperduto[12,6], M.-C. Sutera[6], and A. Turinge[13]

[1] IN2P3, Laboratoire de Physique Subatomique et de Cosmologie, 38026 Grenoble, France
[2] Dipartimento di Fisica, Università di Roma "Tor Vergata", via della Ricerca Scientifica 1, I-00133 Roma, Italy
[3] Dipartimento di Fisica Sperimentale, Università di Torino, via P. Giuria, I-00125 Torino, Italy
[4] INFN - Laboratori Nazionali di Frascati, via E. Fermi 40, I-00044 Frascati, Italy
[5] INFN - Laboratori Nazionali del Sud, via Santa Sofia 44, I-95123 Catania, Italy
[6] INFN - Sezione di Catania, via Santa Sofia 64, I-95123 Catania, Italy
[7] INFN - Sezione di Genova, via Dodecanneso 33, I-16146 Genova, Italy
[8] INFN - Sezione di Roma, piazzale Aldo Moro 2, I-00185 Roma, Italy
[9] INFN - Sezione di Roma Tor Vergata, via della Ricerca Scientifica 1, I-00133 Roma, Italy
[10] INFN - Sezione di Torino, I-10125 Torino, Italy
[11] Istituto Superiore di Sanità, viale Regina Elena 299, I-00161 Roma, Italy
[12] Dipartimento di Fisica ed Astronomia, Università di Catania, via Santa Sofia 64, I-95123 Catania, Italy
[13] Institute for Nuclear Research, 117312 Moscow, Russia
[14] IN2P3, Institut de Physique Nucléaire, 91406 Orsay, France

Received: 7 July 2006 / Revised: 14 December 2006
Published online: 24 January 2007 –
Communicated by N. Bianchi

Abstract. Beam asymmetries and hyperon recoil polarizations for the reactions $\gamma p \to K^+\Lambda$ and $\gamma p \to K^+\Sigma^0$ have been measured from the threshold production to 1500 MeV with the GRAAL facility located at the ESRF in Grenoble. These results complement the database for the beam asymmetry, covering for the first time the production threshold region. Recent theoretical analyses are presented for which the beam asymmetry data bring interesting new information and allow to better determine some resonance parameters. Most importantly, these results strengthen the need of a new D_{13} state around 1900 MeV.

PACS. 13.60.Le Meson production – 13.88.+e Polarization in interactions and scattering – 25.20.Lj Photoproduction reactions

1 Introduction

Until recently, data on kaon photoproduction reactions in the resonance region, because of an intrinsic experimental difficulty, were scarce and had low precision. As a consequence, resonance couplings to either $K\Lambda$ or $K\Sigma$ were poorly known [1]. With the recent release of high-quality data by SAPHIR [2], CLAS [3,4] and LEPS [5,6], a new breakthrough has been achieved in the common endeavour to complete the meson photoproduction database. Several theoretical analyses [7–14] of these new data have been performed. All suggest that new resonances should be incorporated in the nucleon spectrum. They also underline the importance of polarization observable measurements in order to resolve ambiguities in the multipole extraction and make their conclusions stronger.

In the present work, we report on measurements of the beam asymmetry Σ and hyperon recoil polarization P for the reactions $\gamma p \to K^+\Lambda$ and $\gamma p \to K^+\Sigma^0$, over large energy (from threshold to 1500 MeV) and angular ($\theta_{cm} = 30$–140°) ranges. For the first time, the region below 1500 MeV is extensively covered with high-precision Σ data.

[a] e-mail: lleres@lpsc.in2p3.fr
[b] *Present affiliation:* ENEA - C.R. Casaccia, via Anguillarese 301, I-00060 Roma, Italy.
[c] *Present affiliation:* IN2P3, Centre de Spectrométrie Nucléaire et de Spectrométrie de Masse, 91405 Orsay, France.

2 The experimental set-up

2.1 General description

The experiment has been carried-out with the GRAAL facility (see [15] for a detailed description), installed at the European Synchrotron Radiation Facility (ESRF) in Grenoble (France). The tagged and polarized γ-ray beam is produced by Compton scattering of laser photons off the 6.03 GeV electrons circulating in the storage ring.

In the present experiment, we have used a set of UV lines at 333, 351 and 364 nm produced by an Ar laser, giving 1.40, 1.47 and 1.53 GeV maximum energies, respectively. Some data were also taken with the green line at 514 nm (maximum energy of 1.1 GeV).

The photon energy is provided by an internal tagging system. The position of the scattered electron is measured by a silicon microstrip detector (128 strips with a pitch of 300 μm and 1000 μm thick). The energy resolution of the tagging system is 16 MeV (FWHM). A set of plastic scintillators used for time measurements is placed behind the microstrip detector. Thanks to specially developed electronics which synchronize the detector signal with the RF of the machine, the resulting time resolution is ≈ 100 ps. The coincidence between detector signal and RF is used as a start for all Time-of-Flight (ToF) measurements and is part of the trigger of the experiment.

The γ-ray beam polarization is calculated using the expression derived by Arutyunian *et al.* [16] from the Klein-Nishina formula. The UV beam polarization is close to 1 at the maximum energy and decreases smoothly with energy to around 60% at the $K\Lambda$ threshold (0.911 GeV). Based on detailed studies [15], it was found that the only significant source of error for the γ-ray polarization P_γ comes from the laser beam polarization:

$$\frac{\delta P_\gamma}{P_\gamma} = \frac{\delta P_L}{P_L} = 0.02\,. \qquad (1)$$

The γ-ray beam flux (typically 10^6 Hz) is measured by a thin monitor made of three plastic scintillators, yielding an efficiency of around 3%.

The target cell consists of an aluminum hollow cylinder of 4 cm in diameter closed by thin mylar windows (100 μm) at both ends. Two different target lengths (6 and 12 cm) have been used for the present experiment. The target was filled by liquid hydrogen at 18 K ($\rho \approx 7\ 10^{-2}$ g/cm^3).

The 4π LAγRANGE detector of the GRAAL set-up allows to detect both neutral and charged particles (fig. 1). The apparatus is composed of two main parts: a central one ($25^\circ \leq \theta \leq 155^\circ$) and a forward one ($\theta \leq 25^\circ$). In the following, all resolutions are given as the Full-Width Half Maximum (FWHM).

The charged-particles tracks are measured by a set of MultiWire Proportional Chambers (MWPCs). This tracking detector is described in detail in the following section.

Charged-particle identification in the central region is obtained by dE/dx technique thanks to a plastic scintillator barrel (32 bars, 5 mm thick, 43 cm long) with an energy resolution $\approx 20\%$. For the charged particles emitted in the forward direction, a time-of-flight measurement is provided by a double plastic scintillator hodoscope ($300 \times 300 \times 3$ cm^3) placed at a distance of 3 m from the target and having a resolution of ≈ 600 ps. The latter detector provides also a measure of the energy loss dE/dx. Energy calibrations were extracted from the analysis of the $\pi^0 p$ photoproduction reaction while the ToF calibration of the forward wall was obtained from fast electrons produced in the target.

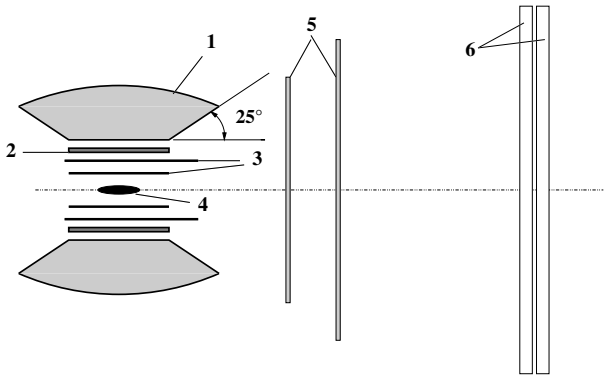

Fig. 1. Schematic view of the LAγRANGE detector: BGO calorimeter (1), plastic scintillator (2), cylindrical MWPCs (3), target (4), plane MWPCs (5), double plastic scintillator hodoscope (6) (the drawing is not to scale).

γ-rays are detected in a BGO calorimeter made of 480 ($15\theta \times 32\varphi$) crystals, each of 21 radiation lengths so that the associated electromagnetic shower is fully contained in the calorimeter. They are identified as clusters of adjacent crystals with no associated hit in the barrel. For the low-energy photons coming from the Σ^0 decay, the cluster multiplicity is 2 on average for an energy threshold of 10 MeV per crystal. The measured photon energy resolution is 3% on average [17–19]. For a thin target, the angular resolution is 6° and 7° for polar and azimuthal angles, respectively ($E_\gamma \geq 200$ MeV). The polar resolution strongly depends on the target length but can be improved using the vertex information given by the tracking detector.

2.2 The tracking detector

For reactions with long-lived particles such as the Λ and/or experiments with extended target, the assumption that the particles are emitted from the centre of the target induces systematic uncertainties on the reconstructed polar angles. In the absence of a magnetic field, our analysis relies entirely on the track information. Consequently, a tracking detector measuring at least two points of the charged-particle trajectories is required.

2.2.1 Forward region

To cover forward angles, two plane chambers, each composed of two planes of wires, are used. To resolve the am-

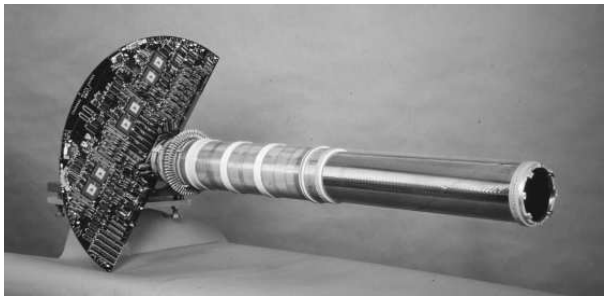

Fig. 2. Picture of the internal cylindrical chamber after removing the external cathode. The entire read-out electronics (strip ADCs and wire counters), based on specially designed ASIC modules, is located on boards directly hooked up to the detector. One of this board, treating half of the signals, is visible on the left-hand side of the picture.

biguities when several particles are emitted in the forward direction, the second chamber is tilted by 45°.

The two plane chambers are placed at 94 and 134 cm from the target centre and have 2×320 and 2×384 wires (3 mm spacing), respectively. The gas is an argon-ethane mixture (85 and 15%).

A track is defined by the association of two hits, one in each chamber. In case of multiple hits, a homothetic projection is used to find the right association.

The detection efficiency of a track is about 95% and the average polar and azimuthal resolutions are 1.5° and 2°, respectively.

2.2.2 Central region

The central region is covered by two coaxial cylindrical MWPCs. Anode wires are stretched parallel to the cylinder's axis and are surrounded by two striped cathodes to measure the induced-charge distribution (figs. 2 and 3). The diameters of the internal and external chambers are 10 and 17 cm, respectively and the corresponding numbers of wire are 128 and 192. Strips are 3.5 mm wide and have a helicoidal shape with opposite pitches for both cathodes. The gas mixture is the same as for the plane chambers.

The track reconstruction is more involved than for the plane chambers and consists of three steps (see [20] for more details):

- Cluster identification and barycentre calculation for the cathode strips.
- Wire-cathode association: for each chamber, the intersection (z-coordinate) between hit wires and strip clusters is calculated by combining information of the two cathodes to select the correct association in case of multiple hits.
- Internal-external chamber association: a criterion based on the φ difference is used to associate the hits in the two chambers and to calculate the parameters of the tracks.

This paper deals only with polarization observables, so no systematic study of efficiencies has been undertaken for multiple charged-particles final states. Single track efficiencies have been nevertheless extracted for $\pi^0 p$ and $\pi^+ n$ reactions and were found to be $\geq 90\%$, in agreement with the simulation. Angular resolutions were also estimated via simulation, giving 3.5° in θ and 4.5° in φ.

Fig. 3. Detailed view of the tip of the internal cylindrical chamber showing the helicoidal strips and the wires. The pitch angle of the strips is 34°.

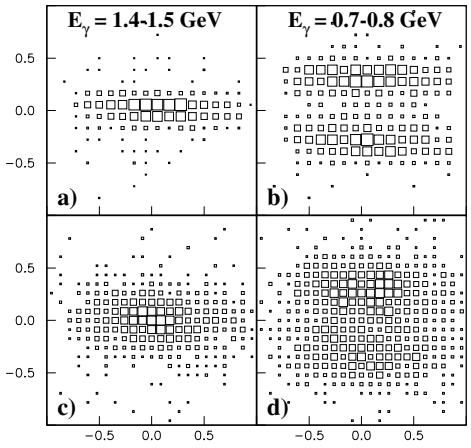

Fig. 4. Transverse beam profile at the target for two photon energy ranges and for the horizontal polarization state. Spectra measured with the cylindrical MWPCs (c, d) are compared to the expected beam profile (a, b). The observed smearing between (a, b) and (c, d) comes from the vertex reconstruction resolution. The scales are in cm.

2.2.3 Vertex reconstruction

In order to check the reliability of the track reconstruction (detector+algorithm), we have taken advantage of the huge statistics cumulated for the $p\pi^+\pi^-$ channel, the most abundant three charged-particles reaction. Figures 4 and 5 show the transverse and longitudinal vertex distributions for this reaction, as measured by the central tracking detector (all particles detected in the cylindrical chambers).

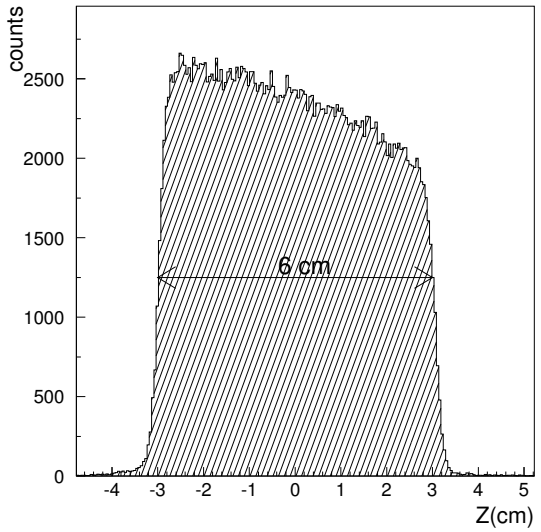

Fig. 5. Longitudinal target profile reconstructed from the vertex distribution of the $p\pi^+\pi^-$ reaction in the case of a 6 cm long target.

The transverse distributions (fig. 4) exhibit the well-known energy and polarization dependences of the Compton scattering γ-ray beam (see [15] and references therein). Moreover, the precise measurement of the beam position could be extracted and used to monitor its small fluctuations run by run.

On the other hand, the longitudinal distribution (fig. 5) reflects the profile of the target and allows one to check the position of the target along the beam axis.

From these spectra, a resolution of 5 mm in the three directions has been extracted.

In the case of $K\Lambda$ and $K\Sigma^0$ reactions, an additional check could be performed. As it will be presented in sect. 3.1.2, the calculated distance between the primary (reaction) and secondary (Λ decay) vertices has been used to reconstruct the Λ lifetime distribution which agrees well with the expected value.

3 Data analysis

3.1 Event selection

For the present analysis, the charged decay of the Λ ($\Lambda \to p\pi^-$, BR = 63.9%) has been considered and, consequently, events with only three tracks were selected. Among these, events containing at most one neutral cluster detected in the BGO calorimeter were retained and sorted into two sub-samples: those with a single neutral particle were associated to the $K\Sigma^0$ ($\Sigma^0 \to \Lambda\gamma$) channel and the others to $K\Lambda$. Each sub-sample was then analysed according to the expected kinematics.

In the absence of a direct measurement of energy and/or momentum of the charged particles, the angles (θ, φ) of the three tracks were combined with kinematical constraints to calculate momenta. Particle identification was then obtained from the association of the calculated momenta with $\mathrm{d}E/\mathrm{d}x$ and/or ToF measurements.

3.1.1 Kinematic analysis

Two different methods have been developed to identify the charged particles and calculate their momenta from the measured angles using the energy momentum conservation of the $K\Lambda$ reaction [21,22].

The first one is based on the three-body kinematics and leads to a system of three linear equations with the three momenta as unknowns. It should be noted that, whenever the three particles are coplanar, this system has no solution.

The second one relies on the two-body nature of the two sequential steps of the reaction: i) $K\Lambda$ production, ii) Λ decay in $p\pi^-$. This method generates a set of second-order equations with multiple solutions for the momenta. The energy balance is used as criterion to select the right solution. While this method avoids event losses due to coplanarity, a possible misidentification can occur.

Thanks to the complete measurement of the Σ^0 decay photon, these methods could be applied in the same way for the $K\Sigma^0$ channel.

3.1.2 Selection cuts

For both channels, the main source of background is the $\gamma p \to p\pi^+\pi^-$ reaction, a channel with a similar final state and a cross-section hundred times larger. For $K\Sigma^0$, an additionnal background contribution comes from $\gamma p \to p\pi^+\pi^-\pi^0$.

To select events, narrow cuts were applied on the following set of experimental quantities:

- Energy balance.
- Effective masses of the three particles extracted from the combination of measured $\mathrm{d}E/\mathrm{d}x$ and ToF (only at forward angles) with calculated momenta.
- Missing mass $m_{\gamma p-K^+}$ evaluated from E_γ, θ_K (measured) and p_K (calculated).
- For $K\Sigma^0$, an additional constraint comes from the decay photon emitted with an energy of 76.96 MeV in the Σ^0 rest frame.

For each of these variables, the width σ of the corresponding distribution (Gaussian-like shape) has been extracted from a Monte Carlo simulation [15] of the apparatus response based on the GEANT3 package of the CERN library.

To check the quality of the event selection, the distribution of the Λ decay length was used due to its high sensitivity to background contamination.

Event by event, track information and Λ momentum were combined to obtain the distance d between the reaction and decay vertices. The Λ decay length was then calculated with the usual formula $ct_\Lambda = d/(\beta_\Lambda * \gamma_\Lambda)$. Figure 6 shows the resulting distributions for events selected with

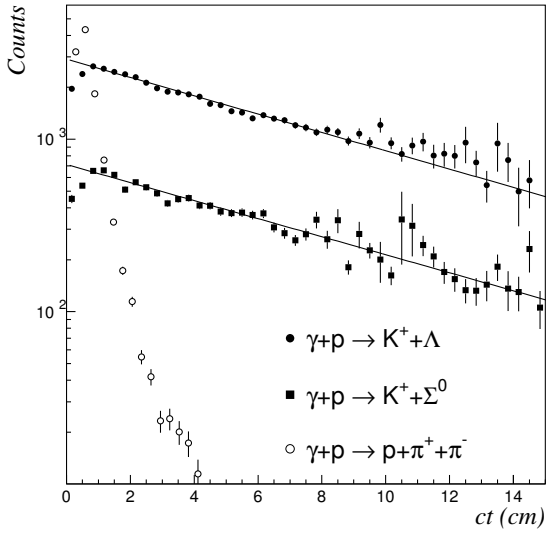

Fig. 6. Reconstructed Λ decay length spectra for the reactions $\gamma p \to K^+\Lambda$ (closed circles) and $\gamma p \to K^+\Sigma^0$ (closed squares). These spectra correspond to events with at least two tracks in the cylindrical chambers. The solid lines represent fits with an exponential function $\alpha * \exp(-ct/c\tau)$ where α and $c\tau$ are free parameters. The last distribution (open circles) has been obtained without applying selection cuts for the $K\Lambda$ reaction. It corresponds to the main background reaction ($\gamma p \to p\pi^+\pi^-$) which, as expected, contributes only to small ct values.

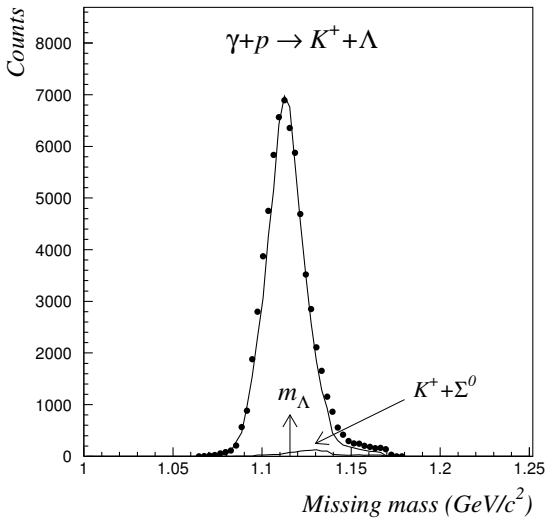

Fig. 7. Distribution of the missing mass $m_{\gamma p-K^+}$ reconstructed from measured E_γ and θ_K and calculated p_K for the reaction $\gamma p \to K^+\Lambda$. Data after all selection cuts (closed circles) are compared to the simulation (solid line). The expected contribution from the reaction $\gamma p \to K^+\Sigma^0$ is also plotted (note that it is not centered on the Σ^0 mass due to kinematical constraints in the event analysis). The vertical arrow indicates the Λ mass.

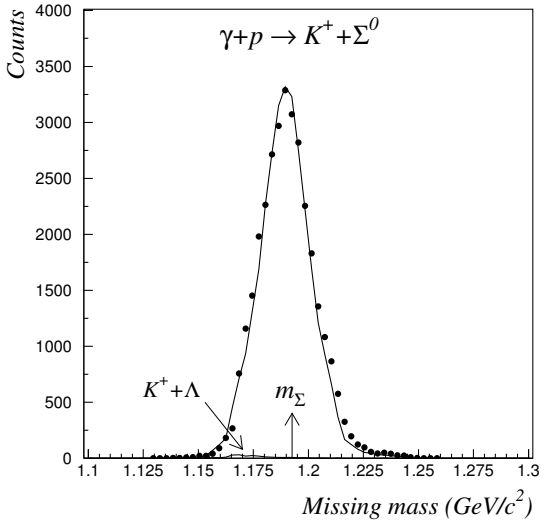

Fig. 8. Distribution of the missing mass $m_{\gamma p-K^+}$ reconstructed from measured E_γ and θ_K and calculated p_K for the reaction $\gamma p \to K^+\Sigma^0$. Data after all selection cuts (closed circles) are compared to the simulation (solid line). The expected contribution from the reaction $\gamma p \to K^+\Lambda$ is also plotted (not centered on the Λ mass). The vertical arrow indicates the Σ^0 mass.

all cuts at $\pm 2\sigma$ ($K\Lambda$: closed circles; $K\Sigma^0$: closed squares) compared with events without cuts (open circles). These spectra have been corrected for detection efficiency losses estimated from the Monte Carlo simulation (significant only for $ct \geq 5\,\mathrm{cm}$). It should be noted that the deficit in the first bins is attributed to finite-resolution effects not fully taken into account in the simulation.

The first two spectra have been fitted for $ct \geq 1\,\mathrm{cm}$ by an exponential function $\alpha * \exp(-ct/c\tau)$ with α and $c\tau$ as free parameters. The fitted $c\tau$ values ($8.17 \pm 0.31\,\mathrm{cm}$ for $K\Lambda$ and $8.30 \pm 0.54\,\mathrm{cm}$ for $K\Sigma^0$) are in good agreement with the PDG expectation for the Λ mean free path ($c\tau_\Lambda = 7.89\,\mathrm{cm}$) [1].

By contrast, the spectrum without cuts is dominated by $p\pi^+\pi^-$ background events. As expected, they contribute mostly to small ct values ($\leq$ 2–3 cm), making the shape of this distribution highly sensitive to background contamination. For instance, a pronounced peak already shows up when opening selection cuts at $\pm 3\sigma$.

A remaining source of background, which cannot be seen in the ct plots presented above, could originate from the crossed contamination between the reactions $\gamma p \to K^+\Lambda$ and $\gamma p \to K^+\Sigma^0$. From the simulation, this mutual contamination was found to be of the order of 2% in the $K\Lambda$ sample of events and less than 1% in the $K\Sigma^0$ one.

As a further check of the quality of the data samples, the missing-mass spectra have been calculated. One should remember that the missing mass is not directly measured and is not used as a criterion for the channel identification. The spectra presented in figs. 7 and 8 for the $K\Lambda$ and $K\Sigma^0$ reactions (closed circles) are in fair agreement with the simulated distributions (solid line). Some slight discrepancies can nevertheless be seen in the high-energy tail of the spectra. The simulated missing-mass distributions of the crossed contamination, also displayed in figs. 7 and 8, clearly indicate that such a background cannot account for the observed differences. Rather, they are attributed to the summation of a large number of data

taking periods with various experimental configurations (target length, wire chambers, green *vs.* UV laser line, ...). Although these configurations were implemented in corresponding simulations, small imperfections (misalignments in particular) could not be taken into account.

To summarize, thanks to these experimental checks, we are confident that the level of background in our samples is low. This is corroborated by the simulation from which a global background contamination (multi-pions and crossed contributions) of the order of 5% was estimated.

3.2 Measurement of Σ

The beam asymmetry Σ was determined from the standard expression (see [15] for more details):

$$\frac{\tilde{N}_V(\varphi) - \tilde{N}_H(\varphi)}{\tilde{N}_V(\varphi) + \tilde{N}_H(\varphi)} = P_\gamma \Sigma \cos(2\varphi), \tag{2}$$

where $\tilde{N}_V$ and $\tilde{N}_H$ are the azimuthal yields normalized by the integrated flux for the vertical and horizontal polarization states, respectively. P_γ is the degree of linear polarization of the beam and φ the azimuthal angle of the reaction plane. Σ was extracted from the fit of the normalized ratio (eq. (2)) by the function $P_\gamma \Sigma \cos(2\varphi)$, using the known energy dependence of P_γ. Two typical examples are given in fig. 9.

This method, based on a ratio, allows one to get rid of many systematic uncertainties. Only two sources of systematic errors have been taken into account: the laser beam polarization (eq. (1)) and the hadronic background. The latter contribution has been estimated from the variation of the extracted asymmetries when cuts are changed from $\pm 2\sigma$ to $\pm 2.5\sigma$. All systematic and statistical errors have been summed quadratically.

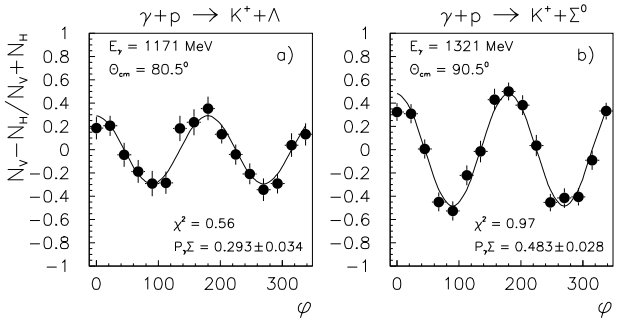

Fig. 9. Azimuthal distributions of the normalized ratio $\tilde{N}_V - \tilde{N}_H/\tilde{N}_V + \tilde{N}_H$: a) $\gamma p \to K^+\Lambda$ reaction at $E_\gamma = 1171$ MeV and $\theta_{cm} = 80.5°$ b) $\gamma p \to K^+\Sigma^0$ reaction at E_γ=1321 MeV and $\theta_{cm} = 90.5°$. The solid lines represent the fits by the function $P_\gamma \Sigma \cos(2\varphi)$ (eq. (2)). The results for $P_\gamma \Sigma$ and the reduced χ^2 values are given.

3.3 Measurement of P

For the reaction $\gamma p \to K^+\Lambda \to K^+ p\pi^-$, with an unpolarized beam, the recoil polarization of the Λ, P_Λ, is necessarily perpendicular to the reaction plane and can be directly measured from the angular distribution of the decay proton [23]:

$$W(\cos\theta_p) = \frac{1}{2}\big(1 + \alpha P_\Lambda \cos\theta_p\big), \tag{3}$$

where $\alpha = 0.642 \pm 0.013$ [1] is the Λ decay parameter and θ_p the angle between the proton direction and the normal to the reaction plane in the Λ rest frame.

For the reaction $\gamma p \to K^+\Sigma^0 \to K^+\Lambda\gamma \to K^+ p\pi^-\gamma$, the polarization vector of the Σ^0, $\mathbf{P}_{\Sigma^0}$, is related to the polarization vector $\mathbf{P}_\Lambda$ of the decay Λ according to [24]:

$$\mathbf{P}_\Lambda = -(\mathbf{P}_{\Sigma^0} \cdot \mathbf{u}_\Lambda)\mathbf{u}_\Lambda\,, \tag{4}$$

where $\mathbf{u}_\Lambda$ is the unit vector along the direction of emission of Λ in the Σ^0 rest frame. Λ is longitudinally polarized in the Σ^0 rest frame. Averaging over all Λ flight directions $\mathbf{u}_\Lambda$ yields to:

$$\langle \mathbf{P}_\Lambda \rangle = -\frac{1}{3}\mathbf{P}_{\Sigma^0}. \tag{5}$$

The angular distribution of the decay proton reduces to

$$W(\cos\theta_p) = \frac{1}{2}\left(1 - \frac{1}{3}\alpha P_{\Sigma^0}\cos\theta_p\right), \tag{6}$$

where θ_p is again the angle between the proton direction in the Λ rest frame and the normal to the reaction plane.

The recoil polarizations P_Λ and P_{Σ^0} have been determined directly from the proton up/down asymmetries with respect to the reaction plane, given by integration of eqs. (3) and (6):

$$P_\Lambda = +\frac{2}{\alpha}\frac{N_{up} - N_{down}}{N_{up} + N_{down}}\,, \tag{7}$$

$$P_{\Sigma^0} = -\frac{6}{\alpha}\frac{N_{up} - N_{down}}{N_{up} + N_{down}}\,, \tag{8}$$

where N_{up} and N_{down} are the number of events with $\cos\theta_p > 0$ and $\cos\theta_p < 0$, respectively. This calculation assumes that the corresponding detection efficiencies are the same, *i.e.* $\epsilon_{up} = \epsilon_{down}$, a reasonable assumption given the cylindrical symmetry of our 4π detector.

The global up/down symmetry of our set-up has been checked via the Monte Carlo simulation of both polarized and unpolarized Λ/Σ^0 decays. For unpolarized decays, the N_{up}/N_{down} ratio was found, as expected, to be close to 1 for all energy and angular bins; for polarized decays, the recalculated asymmetry always agreed with the input value, within a few percent.

An alternative method to extract P consists in fitting the efficiency corrected angular distribution and we did check that it gives results compatible with the previous one for all bins. Nevertheless, for the most forward kaon angle and for photon energies greater than 1100 MeV, the

resulting χ^2 were found to be much larger than one, pointing to remaining imperfections of the simulation. Therefore, we have decided to use the more robust up/down method which relies on a basic experimental feature and is much less dependent on the simulation details.

For the recoil polarization observable, the systematic uncertainties on the Λ decay parameter α and on the hadronic background contributions were considered; the latter was estimated in the same way as for the beam asymmetries. In addition, a systematic error of 3% on the up/down efficiency ratio was included. The systematic and statistical errors have been added quadratically.

4 Results and discussions

The complete set of beam asymmetry and recoil polarization data for the $\gamma p \to K^+\Lambda$ and $\gamma p \to K^+\Sigma^0$ reactions is displayed in figs. 10 to 16. These data cover the production threshold region (911–1500 MeV for $K\Lambda$ and 1046–1500 MeV for $K\Sigma^0$) and a large angular range ($\theta_{cm} = 20$–$140°$ for the kaon). Numerical values are listed in tables 1 to 4. Error bars are the quadratic sum of statistical and systematic errors. Data are available via internet [25].

For the two reactions, the data samples correspond to events selected by either of the two kinematical methods described previously. Due to the different ways of implementing energy momentum conservation, the two subsets do not fully overlap (around 50% of overlapping for both reactions). After checking that results obtained for the two subsets were in agreement, they have been merged to maximize statistics.

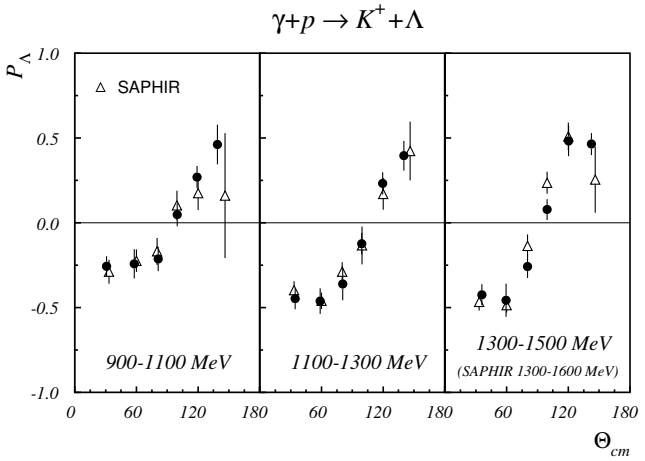

Fig. 10. Λ recoil polarizations for $\gamma p \to K^+\Lambda$. Comparison between GRAAL (closed circles) and SAPHIR (open triangles) data.

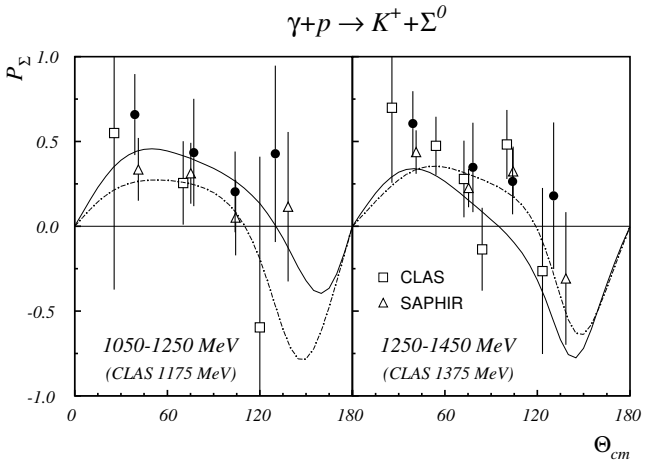

Fig. 11. Σ^0 recoil polarizations for $\gamma p \to K^+\Sigma^0$. Comparison between GRAAL (closed circles), SAPHIR (open triangles) and CLAS (open squares) results. Data are compared with the new (solid line) and the published (dot-dashed line) solutions of the BCC model.

4.1 Comparison to previous results

For the beam asymmetry, our data cover the energy range from threshold to 1500 MeV for the first time. Data have been previously published by the LEPS Collaboration from 1500 to 2400 MeV in the forward region ($\theta_{cm} = 0$–$60°$) [5,6]. A good agreement is observed at 1500 MeV for the two experiments in the narrow angular overlapping region.

Regarding the recoil polarizations, high-quality data produced recently by SAPHIR [2] and CLAS [3] were existing in the same energy and angular ranges. They are compared with the GRAAL data in figs. 10 and 13 for $K\Lambda$ and in fig. 11 for $K\Sigma^0$. For the $K\Lambda$ reaction, the agreement between all experiments is very satisfactory over the full angular range and at all energies. For the $K\Sigma^0$ channel, despite the much larger uncertainties, the overall agreement is fair.

4.2 Discussion

We have compared our results with four models: the dynamical coupled-channel model of Saclay-Argonne-Pittsburgh [10], the Ghent isobar [11] and RPR (Regge-plus-resonance) [12] models and the coupled-channel partial-wave analysis developed by the Bonn-PNPI group [8,9]. In the following, these models will be refered as SAPCC, GI, GRPR and BCC, respectively.

For the $K\Lambda$ reaction, two series of figures have been prepared. In figs. 12 and 13, the published versions of the SAPCC, GI and BCC models are plotted while re-fitted versions of the SAPCC, GRPR and BCC models, after inclusion of our data, are presented in figs. 14 and 15.

For the $K\Sigma^0$ reaction, a specific analysis involving our data was performed only with the BCC model. Figs. 11 and 16 show the published and updated versions of this model.

The SAPCC model [10] is a dynamical coupled-channel formalism. All known resonances are treated in the frame of a chiral constituent quark model, hence limiting the number of adjustable parameters in contrast to isobar models. The model includes the direct $\gamma N \to K\Lambda$ process as well as intermediate πN, $K\Lambda$ and $K\Sigma$ channels.

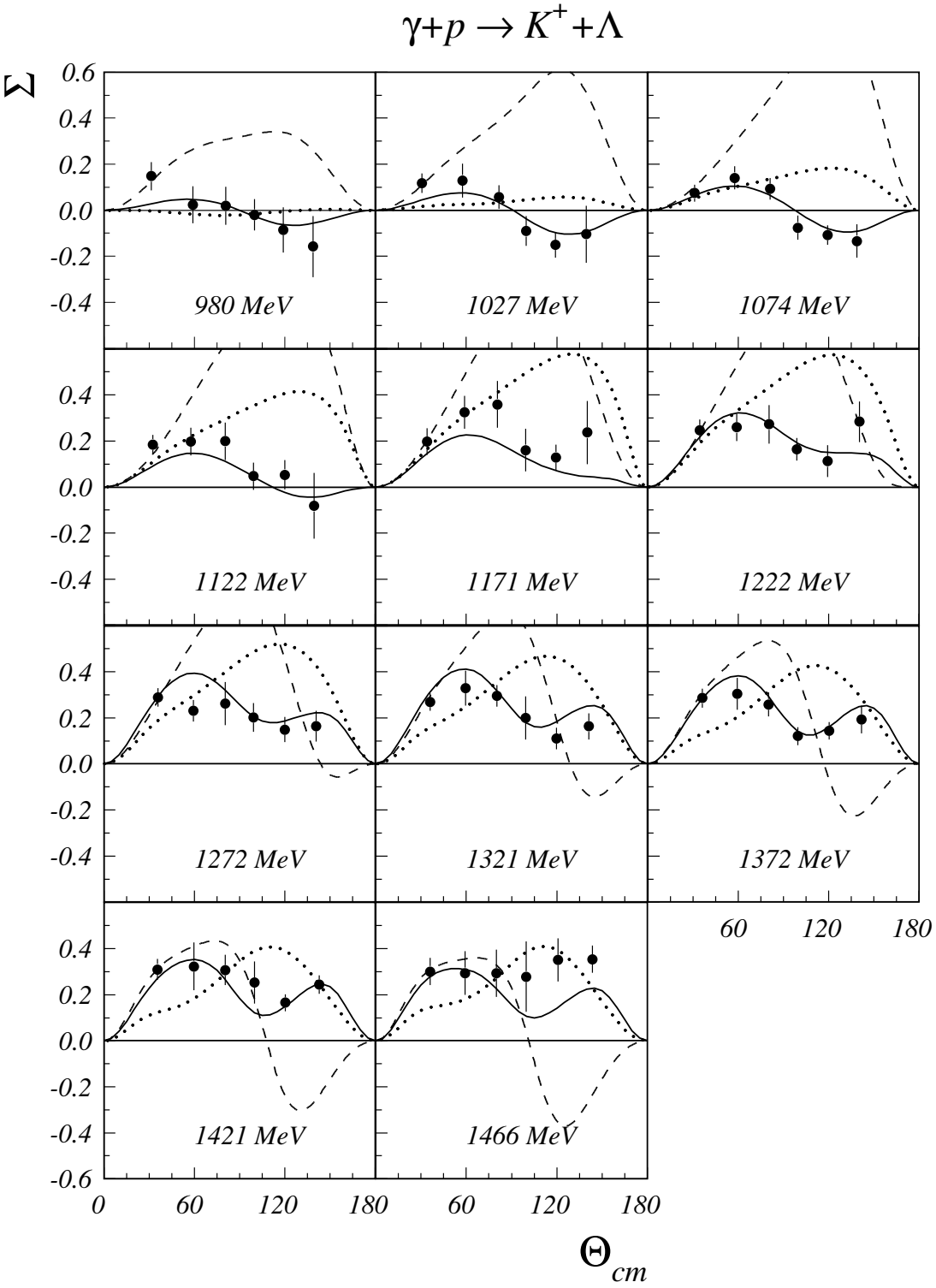

Fig. 12. Angular distributions of the beam asymmetries Σ for $\gamma p \to K^+\Lambda$ and γ-ray energies ranging from threshold up to 1500 MeV. Data are compared with the predictions of the BCC (solid line), SAPCC (dashed line) and GI (dotted line) models.

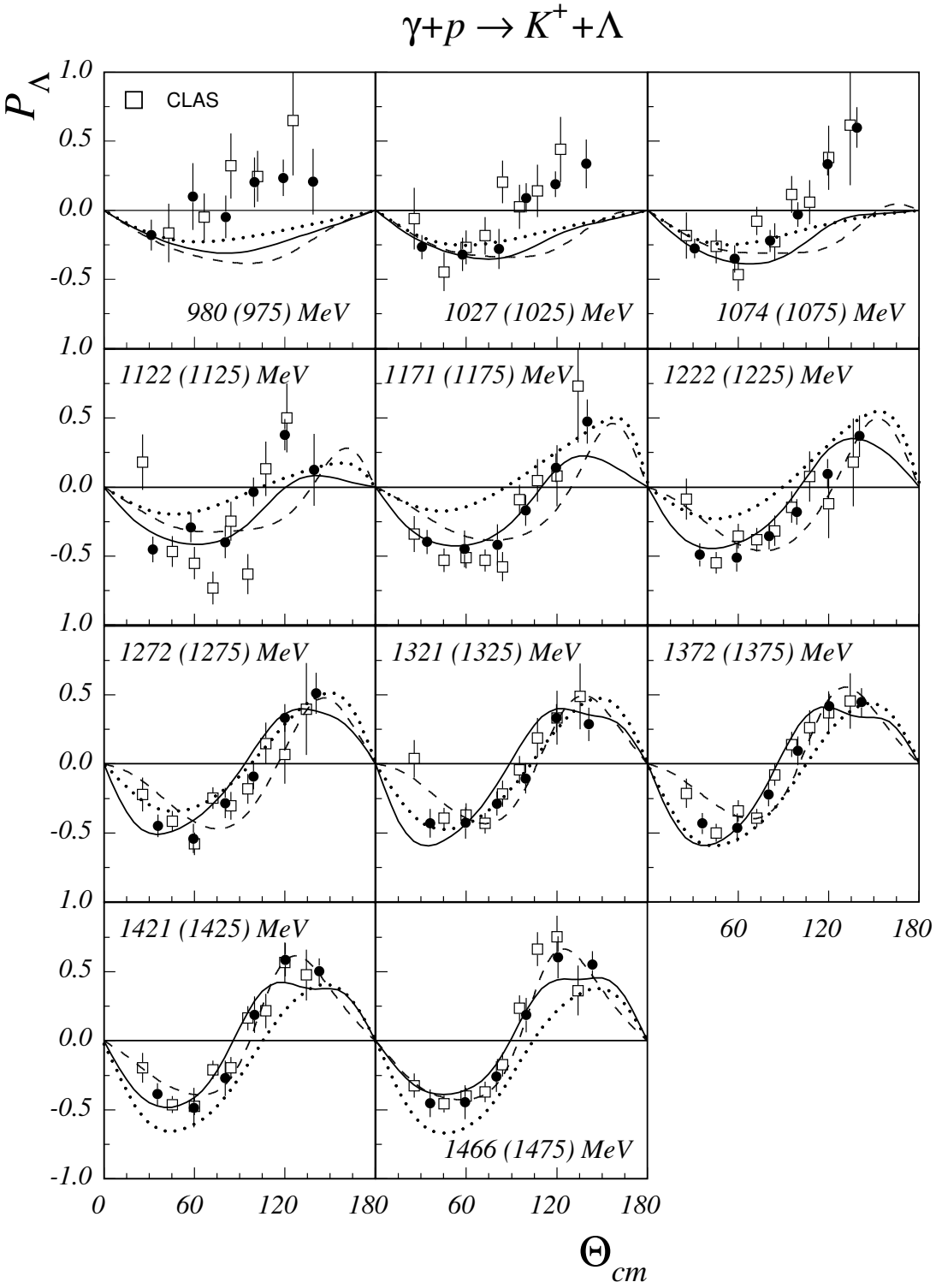

Fig. 13. Angular distributions of the Λ recoil polarizations for $\gamma p \to K^+\Lambda$ and γ-ray energies ranging from threshold up to 1500 MeV. Comparison between GRAAL (closed circles) and CLAS (open squares —energies in parenthesis) results. Data are compared with the predictions of the BCC (solid line), SAPCC (dashed line) and GI (dotted line) models.

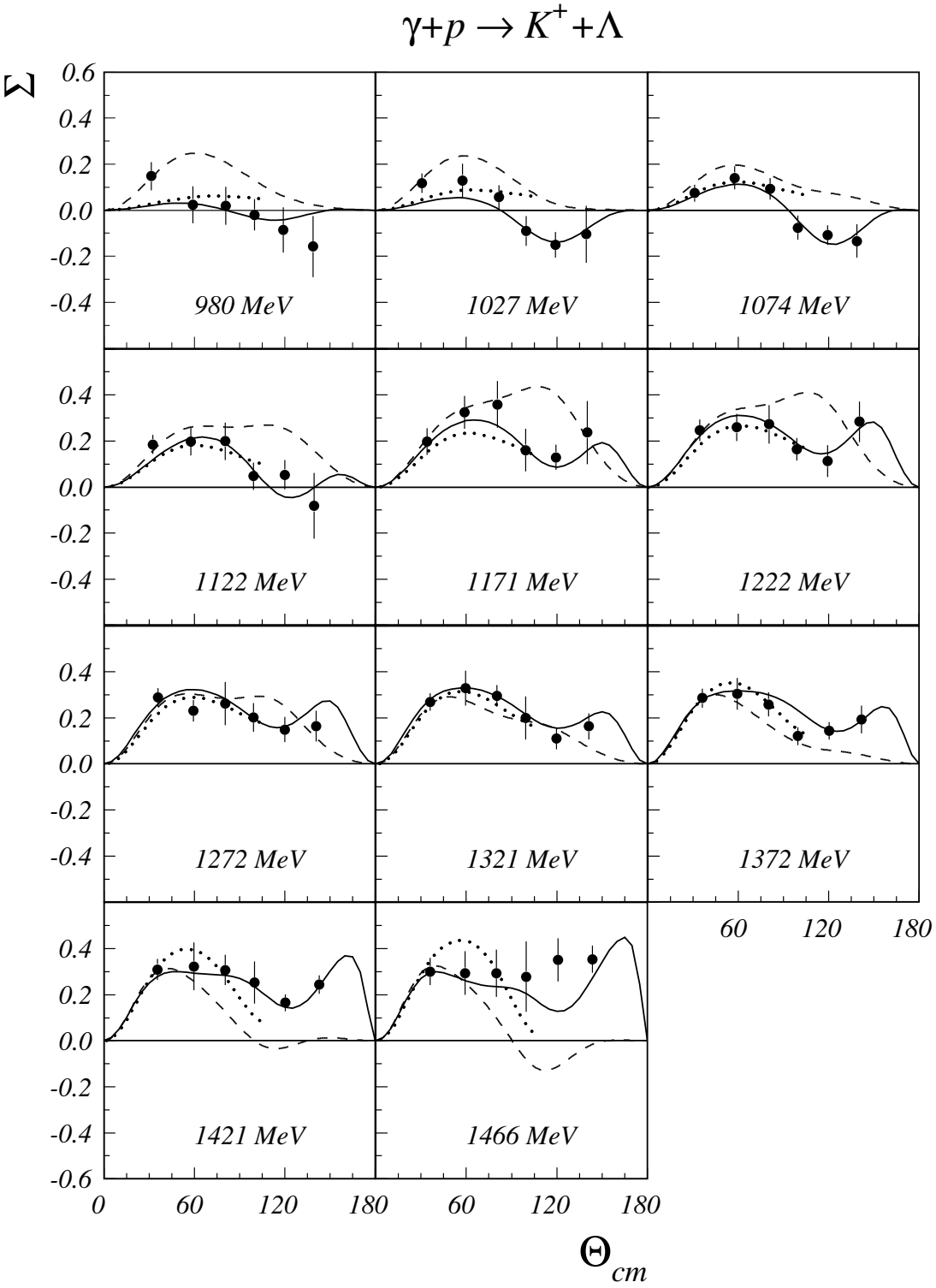

Fig. 14. Angular distributions of the beam asymmetries Σ for $\gamma p \to K^+\Lambda$ and γ-ray energies ranging from threshold up to 1500 MeV. Data are compared with the new solutions of the BCC (solid line), SAPCC (dashed line) and GRPR (dotted line) models.

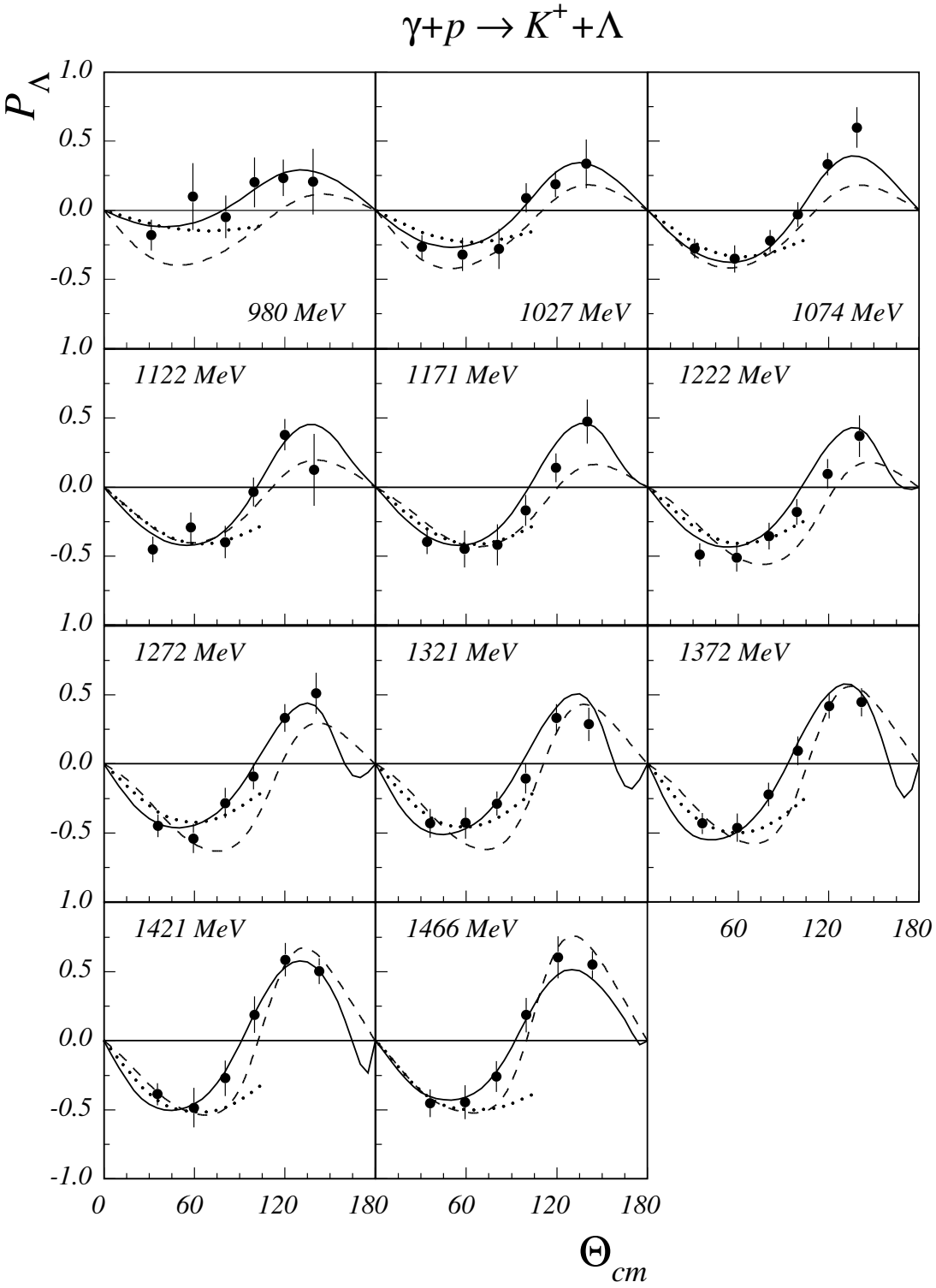

Fig. 15. Angular distributions of the Λ recoil polarizations for $\gamma p \to K^+\Lambda$ and γ-ray energies ranging from threshold up to 1500 MeV. Data are compared with the new solutions of the BCC (solid line), SAPCC (dashed line) and GRPR (dotted line) models.

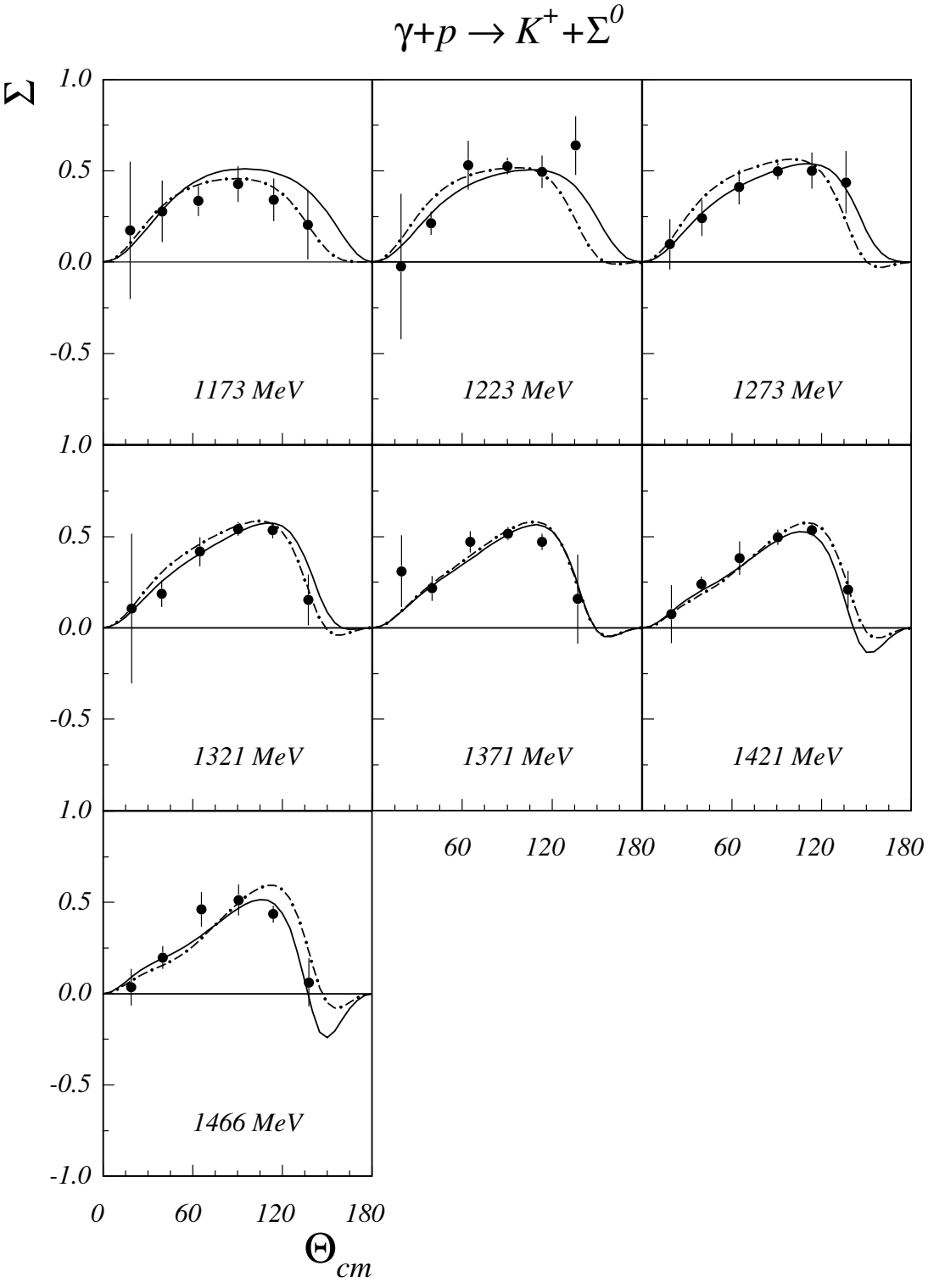

Fig. 16. Angular distributions of the beam asymmetries Σ for $\gamma p \to K^+\Sigma^0$ and γ-ray energies ranging from threshold up to 1500 MeV. Data are compared with the new (solid line) and the published (dot-dashed line) solutions of the BCC model.

Table 1. Beam asymmetries for the reaction $\gamma p \to K^+\Lambda$.

$\theta_{cm}(^\circ)$	$E_\gamma = 980\,\mathrm{MeV}$	$\theta_{cm}(^\circ)$	$E_\gamma = 1027\,\mathrm{MeV}$	$\theta_{cm}(^\circ)$	$E_\gamma = 1074\,\mathrm{MeV}$	$\theta_{cm}(^\circ)$	$E_\gamma = 1122\,\mathrm{MeV}$
31.3	0.148 ± 0.061	30.6	0.117 ± 0.042	31.2	0.074 ± 0.037	32.4	0.185 ± 0.041
59.1	0.025 ± 0.080	57.5	0.129 ± 0.073	57.5	0.141 ± 0.051	57.6	0.198 ± 0.061
80.7	0.018 ± 0.083	81.7	0.057 ± 0.052	81.0	0.094 ± 0.047	80.6	0.199 ± 0.082
99.8	-0.020 ± 0.069	99.8	-0.091 ± 0.064	99.7	-0.076 ± 0.053	99.2	0.048 ± 0.059
118.9	-0.085 ± 0.098	119.0	-0.150 ± 0.056	119.3	-0.108 ± 0.042	119.9	0.054 ± 0.063
138.6	-0.158 ± 0.133	139.5	-0.104 ± 0.124	138.8	-0.134 ± 0.073	139.3	-0.082 ± 0.143
$\theta_{cm}(^\circ)$	$E_\gamma = 1171\,\mathrm{MeV}$	$\theta_{cm}(^\circ)$	$E_\gamma = 1222\,\mathrm{MeV}$	$\theta_{cm}(^\circ)$	$E_\gamma = 1272\,\mathrm{MeV}$	$\theta_{cm}(^\circ)$	$E_\gamma = 1321\,\mathrm{MeV}$
34.1	0.197 ± 0.057	34.6	0.247 ± 0.047	35.8	0.289 ± 0.040	36.0	0.269 ± 0.038
58.9	0.325 ± 0.071	58.9	0.259 ± 0.060	59.2	0.230 ± 0.047	59.4	0.329 ± 0.075
80.5	0.359 ± 0.102	80.4	0.273 ± 0.083	80.6	0.262 ± 0.094	80.3	0.296 ± 0.047
99.3	0.161 ± 0.093	98.9	0.164 ± 0.048	99.2	0.202 ± 0.062	99.2	0.199 ± 0.094
119.4	0.130 ± 0.054	119.1	0.112 ± 0.069	119.9	0.148 ± 0.054	119.9	0.111 ± 0.046
140.4	0.237 ± 0.137	140.3	0.285 ± 0.088	140.8	0.164 ± 0.066	141.3	0.163 ± 0.056

$\theta_{cm}(^\circ)$	$E_\gamma = 1372\,\mathrm{MeV}$	$\theta_{cm}(^\circ)$	$E_\gamma = 1421\,\mathrm{MeV}$	$\theta_{cm}(^\circ)$	$E_\gamma = 1466\,\mathrm{MeV}$
36.1	0.286 ± 0.041	35.7	0.310 ± 0.045	35.9	0.301 ± 0.059
59.5	0.304 ± 0.070	59.6	0.323 ± 0.104	59.3	0.294 ± 0.095
80.1	0.258 ± 0.052	80.3	0.307 ± 0.066	80.0	0.293 ± 0.103
99.4	0.121 ± 0.039	99.7	0.253 ± 0.092	99.7	0.278 ± 0.152
120.4	0.144 ± 0.039	120.4	0.166 ± 0.037	120.8	0.351 ± 0.093
141.9	0.193 ± 0.061	142.8	0.244 ± 0.040	143.7	0.354 ± 0.058

Table 2. Beam asymmetries for the reaction $\gamma p \to K^+\Sigma^0$.

$\theta_{cm}(^\circ)$	$E_\gamma = 1173\,\mathrm{MeV}$	$\theta_{cm}(^\circ)$	$E_\gamma = 1223\,\mathrm{MeV}$	$\theta_{cm}(^\circ)$	$E_\gamma = 1273\,\mathrm{MeV}$	$\theta_{cm}(^\circ)$	$E_\gamma = 1321\,\mathrm{MeV}$
18.1	0.175 ± 0.376	18.9	-0.025 ± 0.399	18.4	0.098 ± 0.138	19.0	0.105 ± 0.411
39.5	0.278 ± 0.169	39.0	0.213 ± 0.064	39.8	0.241 ± 0.097	39.3	0.188 ± 0.072
63.8	0.335 ± 0.082	64.0	0.531 ± 0.134	64.7	0.411 ± 0.094	64.9	0.418 ± 0.080
90.5	0.428 ± 0.097	90.2	0.527 ± 0.046	90.6	0.499 ± 0.047	90.5	0.542 ± 0.038
114.4	0.342 ± 0.117	113.4	0.494 ± 0.089	113.6	0.501 ± 0.099	113.6	0.535 ± 0.044
136.9	0.205 ± 0.189	135.9	0.639 ± 0.161	136.4	0.437 ± 0.171	137.2	0.154 ± 0.139

$\theta_{cm}(^\circ)$	$E_\gamma = 1371\,\mathrm{MeV}$	$\theta_{cm}(^\circ)$	$E_\gamma = 1421\,\mathrm{MeV}$	$\theta_{cm}(^\circ)$	$E_\gamma = 1466\,\mathrm{MeV}$
19.5	0.311 ± 0.197	19.4	0.076 ± 0.159	18.9	0.035 ± 0.099
39.9	0.216 ± 0.069	39.7	0.240 ± 0.042	40.0	0.198 ± 0.062
65.1	0.471 ± 0.058	65.0	0.382 ± 0.092	65.9	0.461 ± 0.094
90.6	0.515 ± 0.036	90.7	0.497 ± 0.041	90.8	0.512 ± 0.084
113.2	0.471 ± 0.046	113.6	0.534 ± 0.033	113.8	0.436 ± 0.046
137.2	0.158 ± 0.244	137.5	0.209 ± 0.102	137.7	0.061 ± 0.132

Inclusion of the $\gamma N \to K\Sigma$ reaction will be done at a later stage and eventually all meson photoproduction data will be treated. The main conclusion drawn from the analysis of the previously published data [5,2–4] (dashed line in figs. 12 and 13) was the necessity to include three new resonances: $S_{11}(1806)$, $P_{13}(1893)$ and $D_{13}(1954)$, the latter one having the most convincing manifestation.

The inclusion of our data in this model started only recently and the conclusions are still preliminary. Nevertheless, some interesting trends have been obtained. Most interestingly, our data strengthen the need for the three new resonances and lead to a reduction of their masses by approximately 100 MeV [26]. Despite a dramatic improvement of the new fit (dashed line in figs. 14 and 15), the overall agreement could still be improved.

The GI model is a standard isobar model for $K\Lambda$ photo- and electroproduction [11]. In addition to the usual Born and kaonic contributions, it includes hyperonic background terms as well as the $S_{11}(1650)$, $P_{11}(1710)$ and $P_{13}(1720)$ nucleon resonances. A number of possible solutions were obtained from the fit to SAPHIR [27], LEPS [5] and Jlab [28] data, containing either a missing $P_{11}(1900)$, $S_{11}(1900)$ or $D_{13}(1900)$ state. Although this model has not been re-fitted to the GRAAL data, the solution with the D_{13} has been found to give the best agreement with our data [29] (dotted line in figs. 12 and 13).

Table 3. Λ recoil polarizations for the reaction $\gamma p \to K^+\Lambda$.

$\theta_{cm}(^\circ)$	$E_\gamma = 980\,\mathrm{MeV}$	$\theta_{cm}(^\circ)$	$E_\gamma = 1027\,\mathrm{MeV}$	$\theta_{cm}(^\circ)$	$E_\gamma = 1074\,\mathrm{MeV}$	$\theta_{cm}(^\circ)$	$E_\gamma = 1122\,\mathrm{MeV}$
31.3	-0.180 ± 0.112	30.6	-0.266 ± 0.088	31.2	-0.277 ± 0.070	32.4	-0.452 ± 0.093
59.1	0.098 ± 0.242	57.5	-0.319 ± 0.122	57.5	-0.352 ± 0.099	57.6	-0.292 ± 0.107
80.7	-0.048 ± 0.153	81.7	-0.280 ± 0.147	81.0	-0.221 ± 0.080	80.6	-0.398 ± 0.118
99.8	0.201 ± 0.182	99.8	0.089 ± 0.106	99.7	-0.032 ± 0.089	99.2	-0.035 ± 0.102
118.9	0.235 ± 0.132	119.0	0.187 ± 0.094	119.3	0.334 ± 0.083	119.9	0.379 ± 0.112
138.6	0.207 ± 0.238	139.5	0.337 ± 0.177	138.8	0.599 ± 0.147	139.3	0.124 ± 0.261
$\theta_{cm}(^\circ)$	$E_\gamma = 1171\,\mathrm{MeV}$	$\theta_{cm}(^\circ)$	$E_\gamma = 1222\,\mathrm{MeV}$	$\theta_{cm}(^\circ)$	$E_\gamma = 1272\,\mathrm{MeV}$	$\theta_{cm}(^\circ)$	$E_\gamma = 1321\,\mathrm{MeV}$
34.1	-0.396 ± 0.087	34.6	-0.490 ± 0.083	35.8	-0.449 ± 0.081	36.0	-0.431 ± 0.105
58.9	-0.450 ± 0.134	58.9	-0.513 ± 0.097	59.2	-0.540 ± 0.106	59.4	-0.428 ± 0.113
80.5	-0.419 ± 0.149	80.4	-0.355 ± 0.096	80.6	-0.283 ± 0.109	80.3	-0.287 ± 0.088
99.3	-0.169 ± 0.111	98.9	-0.179 ± 0.093	99.2	-0.091 ± 0.093	99.2	-0.105 ± 0.108
119.4	0.140 ± 0.104	119.1	0.097 ± 0.107	119.9	0.332 ± 0.101	119.9	0.331 ± 0.103
140.4	0.475 ± 0.162	140.3	0.369 ± 0.151	140.8	0.512 ± 0.148	141.3	0.287 ± 0.121

$\theta_{cm}(^\circ)$	$E_\gamma = 1372\,\mathrm{MeV}$	$\theta_{cm}(^\circ)$	$E_\gamma = 1421\,\mathrm{MeV}$	$\theta_{cm}(^\circ)$	$E_\gamma = 1466\,\mathrm{MeV}$
36.1	-0.431 ± 0.077	35.7	-0.387 ± 0.081	35.9	-0.453 ± 0.102
59.5	-0.463 ± 0.103	59.6	-0.485 ± 0.143	59.3	-0.444 ± 0.123
80.1	-0.221 ± 0.086	80.3	-0.270 ± 0.128	80.0	-0.259 ± 0.112
99.4	0.094 ± 0.104	99.7	0.188 ± 0.132	99.7	0.185 ± 0.125
120.4	0.419 ± 0.089	120.4	0.587 ± 0.122	120.8	0.605 ± 0.152
141.9	0.446 ± 0.101	142.8	0.505 ± 0.093	143.7	0.550 ± 0.100

The GRPR approach [12] is similar to the GI model, except for a Reggeized t-channel background, which is fixed to high-energy data, and the absence of hyperonic contributions. The model presented here contains the same set of usual N^* resonances, plus the $P_{13}(1900)$ state and a missing $D_{13}(1900)$. The resonance couplings were re-fitted to an extended database containing the GRAAL beam asymmetry and recoil polarization data, in addition to the latest CLAS [3,4] and LEPS [5,6] results. Because the Regge parameterization of the background is expected to be most reliable at forward kaon scattering angles, only data with $\theta_{cm} \leq 90^\circ$ were included in the fit, and figures only show results for this angular region. It is found that our data are very discriminating with respect to the particular choice of resonances, especially those in the 1900 MeV mass region [29]. The combination with the $P_{13}(1900)$ and $D_{13}(1900)$ states provides the best global description of the entire dataset (dotted line in figs. 14 and 15).

The BCC model [8,9] is a combined analysis of photoproduction experiments with πN, ηN, $K\Lambda$ and $K\Sigma$ final states [8,9]. Photoproduction data available from SAPHIR [2], CLAS [3] and LEPS [5,30] for the reactions $\gamma p \to K^+\Lambda$, $\gamma p \to K^+\Sigma^0$ and $\gamma p \to K^0\Sigma^+$ were used. Data for π^0 and η photoproduction from CB-ELSA [31, 32], Mainz-TAPS [33] and GRAAL [15,34] as well as results on $\gamma p \to n\pi^+$ [35] were also included. As compared to the other models, the BCC partial-wave analysis takes into account a much larger database.

A good agreement with the whole database has been obtained with 14 N^* and 7 Δ^* resonances. Most baryon resonances were found with masses, widths and electromagnetic amplitudes which are compatible with the PDG compilation [1]. One of the main outcome of this model was the necessity to introduce several new N^* resonances above 1800 MeV. In particular, the analysis demanded the presence of a D_{13} state at 1875 MeV. The published solution has a large contribution from the S_{11} resonances. However, near the threshold, the t- and u-channel exchanges also produce contributions which are mostly S-waves ones, so some ambiguities are inevitable when only non-polarized data are fitted. To resolve such ambiguities the fit of observables which depend mostly on the interferences between amplitudes, *i.e.* polarization observables, is a very important issue. It should be noted that the predictions for Σ and P of the published solution already provide a satisfactory overall agreement for both reactions (solid line in figs. 12, 13 and dot-dashed line in figs. 11, 16).

Table 4. Σ^0 recoil polarizations for the reaction $\gamma p \to K^+\Sigma^0$.

$\theta_{cm}(^\circ)$	$E_\gamma = 1186\,\mathrm{MeV}$ (1050–1250 MeV)	$\theta_{cm}(^\circ)$	$E_\gamma = 1357\,\mathrm{MeV}$ (1250–1450 MeV)
38.9	0.659 ± 0.239	39.1	0.606 ± 0.191
77.2	0.435 ± 0.317	78.1	0.348 ± 0.264
104.0	0.204 ± 0.238	104.0	0.266 ± 0.195
130.1	0.428 ± 0.520	130.5	0.181 ± 0.432

As for the two previous models, the inclusion of the GRAAL data in the fit confirms the need of a new D_{13} state around 1900 MeV. More generally, they help to fix the non-resonant contributions in the BCC model [36] and therefore to better define the resonance parameters. In particular, the beam asymmetry data help a lot to resolve

ambiguities near threshold in the S_{11} multipole. As a result, the final solution has much less contribution from S_{11} resonances and bigger contribution from t-channel exchanges. The quality of the agreement of the new version is excellent (solid line in figs. 11, 14, 15 and 16).

It is particularly striking that all models, while using totally different formalisms as well as fitted database, lead to a common conclusion. They all point to the need for a new D_{13} state around 1900 MeV.

5 Summary

In this paper, we have presented new results for the reactions $\gamma p \to K^+\Lambda$ and $\gamma p \to K^+\Sigma^0$ from threshold to 1500 MeV. Precise measurements for beam asymmetries and hyperon recoil polarizations have been obtained over a wide angular range. These results significantly extend the strangeness photoproduction database and complement the beam asymmetry measurements below 1500 MeV. We have compared our results with four models, which are able to reasonably fit the whole set of data. They all conclude on the need to enrich the nucleon spectrum with several new resonances. Among the various candidates, a new D_{13} state around 1900 MeV appears to be necessary to describe our beam asymmetry data in all discussed models.

We are grateful to A.V. Anisovich, E. Klempt, V.A. Nikonov, A.V. Sarantsev, B. Saghai and T. Corthals for communication of their most recent analyses. It is a pleasure to thank the ESRF as a host institution and its technical staff for the smooth operation of the beam. Technical assistance of all participating institutions is greatly acknowledged, with special mention to A. Pélissier and A. Maurice from LPSC who took charge of the long and delicate construction of the cylindrical chambers.

References

1. *Review of Particle Physics 2004*, Phys. Lett. B **592**, 1 (2004).
2. K.-H. Glander *et al.*, Eur. Phys. J. A. **19**, 251 (2004).
3. J.W.C. McNabb *et al.*, Phys. Rev. C **69**, 042201(R) (2004); R. Schumacher, private communication.
4. R. Bradford *et al.*, Phys. Rev. C **73**, 035202 (2006).
5. R.G.T. Zegers *et al.*, Phys. Rev. Lett. **91**, 092001 (2003).
6. M. Sumihama *et al.*, Phys. Rev. C **73**, 035214 (2006).
7. T. Mart, C. Bennhold, H. Haberzettl, L. Tiator, KAON-MAID isobar model; references and results available at the website `www.kph.uni-mainz.de/MAID`.
8. A.V. Anisovich *et al.*, Eur. Phys. J. A. **25**, 427 (2005).
9. A.V. Sarantsev *et al.*, Eur. Phys. J. A. **25**, 441 (2005).
10. B. Juliá-Díaz, B. Saghai, T.-S.H. Lee, F. Tabakin, Phys. Rev. C **73**, 055204 (2006).
11. D.G. Ireland, S. Janssen, J. Ryckebusch, Nucl. Phys. A **740**, 147 (2004); S. Janssen, J. Ryckebusch, D. Debruyne, T. Van Cauteren, Phys. Rev. C **65**, 015201 (2002).
12. T. Corthals, J. Ryckebusch, T. Van Cauteren, Phys. Rev. C **73**, 045207 (2006).
13. A. Usov, O. Scholten, Phys. Rev. C **72**, 025205 (2005).
14. T. Mart, A. Sulaksono, Phys. Rev. C **74**, 055203 (2006).
15. O. Bartalini *et al.*, Eur. Phys. J. A **26**, 399 (2005).
16. F.R. Arutyunian *et al.*, Teor. Fiz. **45**, 312 (1963).
17. P. Levi Sandri *et al.*, Nucl. Instrum. Methods A **370**, 396 (1996).
18. M. Castoldi *et al.*, Nucl. Instrum. Methods A **403**, 22 (1998).
19. F. Ghio *et al.*, Nucl. Instrum. Methods A **404**, 71 (1998).
20. L. Nicoletti, Thesis, Université J. Fourier (Grenoble) 2002, unpublished.
21. T. Russew, Thesis, Université J. Fourier (Grenoble) 1995, unpublished.
22. P. Calvat, Thesis, Université J. Fourier (Grenoble) 1997, unpublished.
23. T.D. Lee, C.N. Yang, Phys. Rev. **108**, 1645 (1957).
24. R. Gatto, Phys. Rev. **109**, 610 (1958).
25. The full data set is available at the website `http://lpsc.in2p3.fr/GRAAL1`.
26. B. Saghai, private communication.
27. M.Q. Tran *et al.*, Phys. Lett. B **445**, 20 (1998).
28. R.M. Mohring *et al.*, Phys. Rev. C **67**, 055205 (2003).
29. T. Corthals, private communication.
30. R. Lawall *et al.*, Eur. Phys. J. A. **24**, 275 (2005).
31. O. Bartholomy *et al.*, Phys. Rev. Lett. **94**, 012003 (2005).
32. V. Crede *et al.*, Phys. Rev. Lett. **94**, 012004 (2005).
33. B. Krusche *et al.*, Phys. Rev. Lett. **74**, 3736 (1995).
34. J. Ajaka *et al.*, Phys. Rev. Lett. **81**, 1797 (1998).
35. K.H. Althoff *et al.*, Phys. Rev. C **18**, 199 (1983); K. Buechler *et al.*, Nucl. Phys. A **570**, 580 (1994).
36. A.V. Sarantsev, private communication.